

THE SIMULATION OF SECONDARY FLOW EFFECTS IN TURBULENT NON-CIRCULAR PASSAGE FLOWS

C. W. RAPLEY

Department of Mechanical Engineering, Sunderland Polytechnic, Sunderland, England

SUMMARY

A finite difference method has been developed to predict the overall features of the local mean flow in fully developed turbulent non-circular passage flows. The main transport effects of secondary flow have been identified and simulated with diffusion transport in a simple way which eliminates solution of the cross-plane momentum and continuity equations and produces a compact calculation method. Predictions are presented for four different passage shapes and are discussed in relation to experimental measurements and predictions from other more complex methods. Although some minor details were not predicted, the main effects of secondary flow on the mean flow were found to have been quite well simulated, yielding predictions that are in reasonable overall agreement with experiment.

KEY WORDS Fluid Flow Turbulent Non-circular Passages Secondary Flow

1. INTRODUCTION

The design and development of compact passages for heat exchangers, including those in nuclear reactor cores, depends critically on knowledge of the local mean flow and heat transfer characteristics. These characteristics are much influenced by the turbulence-driven secondary flows that occur in the cross-plane of all non-circular passages. These flows cause the main flow to spiral through the passage and although they are relatively weak compared with the main flow, they have a significant influence on the local mean flow distributions of interest, chiefly the axial velocity and wall shear stress.

The main source of information on turbulent passage flows is experiment where, in some cases,¹⁻⁴ detailed measurements of secondary velocities and turbulence have been made.

From these measurements secondary velocities appear to be mainly less than 2 per cent of the mean axial velocity with circulation patterns generally from the core region into the corners, or equivalent regions bounded by converging walls, returning to the core via the wall and wall normals. Figure 1 illustrates the measured flow patterns for square and rectangular ducts and for an equilateral triangular duct. The presence and effect of these secondary motions was recognized by Nikuradse^{5,6} in some of the earliest non-circular duct flow experiments where, as shown in Figure 2, axial velocity contours were found to bulge markedly into the duct corners. These distortions were interpreted as the convective effects of secondary flow and indeed Nikuradse anticipated the circulations shown in Figure 1, although it was more than thirty years before his deductions were confirmed by measurements. The bulging of axial velocity contours into passage corner regions has become a recognized secondary flow effect on the mean flow.

The influence of secondary flow on wall shear stress is even more dramatic than that on

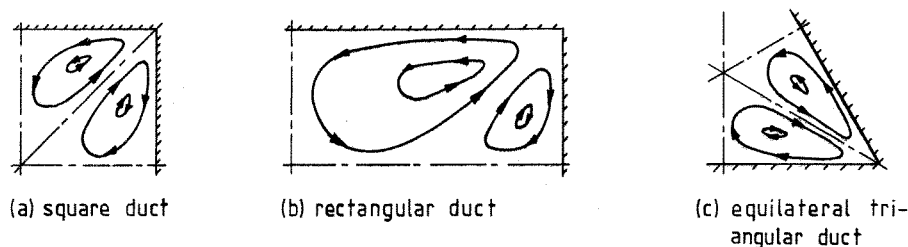
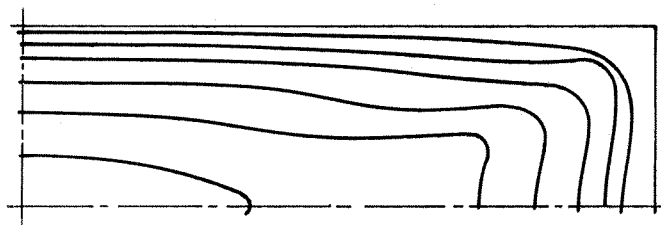


Figure 1. Measured secondary flow patterns

the axial velocity. The convection of core fluid into the corner will increase velocity gradients and thus wall shear stress in the corner wall region. Conversely, convection of the wall region fluid away from the wall in the mid-wall region will decrease axial velocity gradients and thus wall shear stress in the mid-wall region. This has the combined effect of making the wall shear stress more evenly distributed than it would otherwise be. These effects are illustrated in Figure 5(a) for the square duct case where the profile calculated without secondary flow effects is seen to decay monotonically from mid-wall to the corner, whereas the measured profile is much more uniform.

With the almost overwhelming variety of passage shapes that could be of interest and the inherent difficulties of setting up experiments and obtaining reliable measurements, the development of a calculation procedure to supplement experiment will have obvious benefits. Such a procedure could provide useful local data with, for example, a much wider range of geometry and flow conditions than could be contemplated with experiment. It is clear however, that the calculation method must include the effects of secondary flow if local mean flow distributions are to be properly predicted.

Many efforts have been made to develop calculation procedures for particular non-circular passages that include the turbulence driven secondary flows in the passage cross-plane. These procedures mainly used finite differences and were for the square duct and the axial flow passage in rod bundles. A brief overview of these methods is given by Gosman and Rapley,⁷ from which it is evident that such methods may include the simultaneous solution of up to eleven coupled non-linear partial differential equations; the cross-plane momentum and continuity equations and the axial momentum equations account for four of these partial differential equations, the remainder being required for calculation of the Reynolds stresses appearing in the momentum equations. The square duct calculations of Naot *et al.*⁸ and Reece⁹ are examples of the more elaborate of these methods where each required Reynolds stress was obtained from its own partial differential transport (p.d.t.) equation, i.e. the Reynolds stress transport equations. However, in many of the most recent of these finite

Figure 2. Measured⁵ axial velocity contours in a rectangular duct of aspect ratio 3.5

difference methods^{4,7,10-14} the number of p.d.t. equations were reduced by employing simplified algebraic forms of the Reynolds stress transport equations. This algebraic stress transport model (ASTM) was first derived for square duct calculations by Launder and Ying¹⁰ and then further analysed by Gessner and Emery¹⁵ to yield a set of algebraic equations for the complete Reynolds stress tensor in terms of axial velocity gradients, turbulence kinetic energy k and its dissipation rate ϵ .

Calculation methods based on the ASTM have been successfully developed for fully developed flow in particular passage shapes including the square duct,¹⁰ rod bundle passages^{11,12} and an equilateral triangular duct.⁴ In these procedures k was calculated from its modelled p.d.t. equation¹⁶ and ϵ was calculated from the widely used formula obtained from dimensional analysis:¹⁶

$$\epsilon = C_D k^{1.5} / l \quad (1)$$

where C_D is an empirical constant and l a turbulence length scale. The latter was prescribed, either from experimental measurements¹¹ or from the Buleev¹⁷ geometric formula^{4,10}

$$1/l = 0.5 \int_0^{2\pi} d\phi / S \quad (2)$$

where S is the distance to the boundary surface in direction ϕ . The cross-plane p.d.t. equations were cast into stream function and vorticity form to eliminate pressure and solved by finite differences using either Cartesian or polar-cylindrical co-ordinate grids. Considerable difficulties were encountered with convergence of the solutions, due mainly to the coupling and non-linearity of the equations, a feature that was most prominent in the cross-plane Reynolds stresses. In some cases simplifications were made by omitting the cross-plane shear stresses and in others the direction of the secondary flow circulation was prescribed in order to obtain reasonable convergence of the solution.

In the method of Gosman and Rapley,⁷ which was developed for arbitrary shaped ducts, both k and ϵ were calculated from their own p.d.t. equations to avoid any special empirical inputs for particular passage shapes. The p.d.t. equations for momentum, continuity and turbulence were solved directly by finite differences on an orthogonal curvilinear grid generated to fit the passage shape. Convergence difficulties were again encountered, particularly with the cross-plane momentum and continuity equations, where multiple secondary flow circulations could appear in the solution to frustrate convergence. These difficulties were largely overcome however with a combination of special starting conditions and under-relaxation, although much attention needed to be paid to these aspects to ensure converged solutions. The predictions of turbulent flow and heat transfer obtained for various passage shapes and flows generally displayed the expected secondary flow circulations and features and were in reasonable agreement with the available experimental data.

The previous work has shown that ASTM based calculation methods can be successfully used to predict turbulence driven secondary flow and its effects on local mean flow in passages. The present work has arisen from this previous work and seeks to establish whether simplifications can be made to eliminate solution of the cross-plane momentum and continuity equations and produce a procedure that is still capable of predicting the main features of fully developed passage flows including the recognized overall secondary flow effects. The ultimate aim is to develop a calculation procedure that can be applied to any passage shape without special input other than the shape, and that is stable and compact enough to be mounted on the current generation of minicomputers and so be of direct use to

those concerned with the design and development of flow and heat transfer equipment with non-circular passages.

2. THE MATHEMATICAL PROBLEM

2.1. Axial momentum

The axial momentum equation for fully developed turbulent flow in straight passages can be written firstly in Cartesian co-ordinates form for clarity and in terms of effective viscosity μ_{eff} as

$$\partial(\rho uw)/\partial x + \partial(\rho vw)/\partial y = -dp/dz + \partial(\mu_{\text{eff}} \partial w/\partial x)/\partial x + \partial(\mu_{\text{eff}} \partial w/\partial y)/\partial y \quad (3)$$

where velocity components u and v are in cross-plane directions x and y respectively and w is in the axial direction z , p represents pressure and the effective viscosity is given by

$$\mu_{\text{eff}} = \mu_t + \mu \quad (4)$$

The turbulent viscosity μ_t can be calculated from the Prandtl-Kolmogorov formula¹⁸ for generality with passage shape i.e.

$$\mu_t = C_\mu k^2/\varepsilon \quad (5)$$

where C_μ is a constant.

Solution of the axial momentum equation (3) requires values of k and ε for μ_{eff} and of secondary velocity components u and v . The latter would normally require solution of the cross-plane momentum and continuity equations with the attendant stability problems mentioned in the previous section. However, in a wall bounded region and transport effects represented by the two secondary velocity terms on the l.h.s. of equation (3) can be simplified. A study of secondary velocity measurements (see Figure 1) in square ducts,^{1,2} rectangular ducts³ and an equilateral triangular duct⁴ and of calculations which show the convective effect of these flows,⁷ will show that in a wall region, secondary flow normal to the wall is negligible and the region is dominated by flow parallel to the wall. If a wall is assumed parallel to the x direction, then in the l.h.s. of equation (3), the first term dominates the second which can be neglected.

In the present work a gross simplification was then made by replacing the convective transport effect of the first term in equation (3) by diffusive transport i.e.

$$\partial(\rho uw)/\partial x \equiv -\partial(B\mu_{\text{eff}} \partial w/\partial x)/\partial x \quad (6)$$

where B is an empirical constant to be determined. It must be emphasized that there is no theoretical justification for equation (6) since the two transport mechanisms are physically quite different although they both depend on the same stress fields. The simplification was made here since, like the secondary flow, it provided a significant transport effect parallel to the wall and was further expedient in eliminating the difficulties and expense of calculating the recirculating secondary flow. Equation (3) now becomes

$$-dp/dz + \partial(\{1+B\}\mu_{\text{eff}} \partial w/\partial x)/\partial x + \partial(\mu_{\text{eff}} \partial w/\partial y)/\partial y = 0 \quad (7)$$

Equation (7) has a form similar to that obtained with anisotropic effective viscosities with an anisotropy of $(1+B)$ and secondary flow neglected. Calculation methods employing anisotropic eddy viscosities have, of course, been used for passage flows before although mainly for rod bundles. In most cases secondary flow was neglected and anisotropic eddy

viscosities introduced to improve the circumferential coupling of the velocity field. The basis used to fix the distributions and levels of anisotropy were different in each procedure developed. In some cases the levels were postulated (e.g. Vonka and Boonstra¹⁹) whilst in others fairly elaborate models were developed, usually based on different length scales in different directions (e.g. Meyder²⁰) sometimes chosen intuitively (e.g. Ramm and Johansen²¹). The absence of a consistent approach in these and other methods is probably due to the lack of convincing experimental evidence on the anisotropy of eddy viscosities in non-circular duct flows. Attempts at such measurements have been made, either directly or indirectly (e.g. Rehme,²² Kjellstrom,²³ Carajilescov²⁴) but the data is scattered and inconclusive, due most likely to the shear stresses and axial velocity gradients required being dependent on small differences in large measured quantities.

The presence of a wall will certainly cause anisotropy in turbulent fluctuations as evidenced by the higher measured normal stress levels parallel to the wall compared with normal to the wall (e.g. Brundrett and Baines²). However, as also indicated by the latter measurements, such effects are likely to be confined to the local near-wall region and not influenced significantly by flow condition, other walls etc. further away.

The ASTM based calculation methods mentioned in the previous section^{4,7,10-14} used isotropic eddy viscosities with secondary flow and predicted the local mean flow generally satisfactorily. This suggests that anisotropic eddy viscosities may have only a minor effect compared with that of secondary flow. This is the view of Nijsing and Eiffler²⁵ who made rod bundle calculations with prescribed secondary flows and anisotropic eddy viscosities and found secondary flow to have more than three times the effect of anisotropic viscosities on the axial velocity field. It appears therefore that the calculation methods using anisotropic eddy viscosities and neglecting secondary flow may be mainly compensating for the latter neglect of convection transport rather than allowing for any anisotropy in diffusion transport.

The present work takes the viewpoint that anisotropic eddy viscosity effects are minor and so employs isotropic eddy viscosities given by equation (5). The convective transport effects of secondary flow on the velocity field are replaced by diffusive transport to eliminate solution of the cross-plane momentum and continuity equations and so obtain a more compact calculation procedure.

The rod bundle calculations of Trupp and Aly¹² included some tests on the effects of anisotropic turbulent viscosities on wall shear stress. Similar effects were noted to that of secondary flow in making the wall shear stress more uniform and it was further apparent that an assumed uniform anisotropy gave results comparable to the more complex distributions and levels implied by the measurements of Rehme.²² Thus, as a first step in the present work a constant and uniform value of B was assumed to apply throughout the flow field and to be universal to all passage geometries calculated. From a parametric study of a range of geometries the value of $B = 2.5$ was adopted.

2.2. Turbulence equations

The modelled transport equations used to calculate k and ε were the now accepted forms appropriate to high Reynolds number flows in which viscous effects are deemed negligible.^{16,26} For fully developed flow in straight passages they are written in Cartesian form as

$$\partial(\rho uk)/\partial x + \partial(\rho vk)/\partial y = \partial(\{\mu_t/\sigma_k\} \partial k/\partial x)/\partial x + \partial(\{\mu_t/\sigma_k\} \partial k/\partial y)/\partial y + P - \rho\varepsilon = 0 \quad (8)$$

$$\partial(\rho u\varepsilon)/\partial x + \partial(\rho v\varepsilon)/\partial y = \partial(\{\mu_t/\sigma_\varepsilon\} \partial \varepsilon/\partial x)/\partial x + \partial(\{\mu_t/\sigma_\varepsilon\} \partial \varepsilon/\partial y)/\partial y + \varepsilon(C_{\varepsilon 1}P - C_{\varepsilon 2}\rho\varepsilon)/k \quad (9)$$

where σ_k and σ_ε are the turbulent Prandtl (Schmidt) numbers for k and ε respectively, $C_{\varepsilon 1}$

and C_{e2} are constants and P the production rate of k which, neglecting secondary velocity gradients, is given by

$$P = -\overline{\rho u'w'} \partial w / \partial x - \overline{\rho v'w'} \partial w / \partial y \quad (10)$$

The same simplifications were made to the convection transport terms on the l.h.s. of equations (8) and (9) as made in the axial momentum equation yielding:

$$\partial(\{1+B\}\{\mu_t/\sigma_k\} \partial k / \partial x) / \partial x + \partial(\{\mu_t/\sigma_k\} \partial k / \partial y) / \partial y + P - \rho \epsilon = 0 \quad (11)$$

$$\partial(\{1+B\}\{\mu_t/\sigma_\epsilon\} \partial \epsilon / \partial x) / \partial x + \partial(\{\mu_t/\sigma_\epsilon\} \partial \epsilon / \partial y) / \partial y + \epsilon(C_{e1}P - C_{e2}\rho\epsilon) / k = 0 \quad (12)$$

2.3. The equations in orthogonal curvilinear co-ordinates

The p.d.t. equations to be solved have been reduced to diffusive transport equations (7), (11) and (12) which can be written in the following common form:

$$\partial(\{1+B\}D_\phi \partial \phi / \partial x) / \partial x + \partial(D_\phi \partial \phi / \partial y) / \partial y + C_\phi = 0 \quad (13)$$

where ϕ stands for w , k or ϵ and D_ϕ is the diffusion coefficient associated with each ϕ . C_ϕ represents the source and any other terms not contained in the other components.

The Cartesian equation (13) can be transformed to general orthogonal curvilinear co-ordinate form (see for example Pope²⁷) giving an equation of the form

$$\partial(\{h_2/h_1\}\{1+B\}D_\phi \partial \phi / \partial \zeta_1) / \partial \zeta_1 + \partial(\{h_1/h_2\}D_\phi \partial \phi / \partial \zeta_2) / \partial \zeta_2 + C_\phi = 0 \quad (14)$$

where h_1 and h_2 are the metric coefficients in the cross-plane curvilinear co-ordinate

Table I. Coefficients in the general transport equation

ϕ	D_ϕ	C_ϕ
u_3	μ_{eff}	$-h_1 h_2 dp/d\zeta_3$
k	μ_t/σ_k	$h_1 h_2 (P - \rho \epsilon)$
ϵ	μ_t/σ_ϵ	$h_1 h_2 (C_{e1}P - C_{e2}\rho\epsilon) / k$

directions ζ_1 and ζ_2 respectively. Table I summarizes D_ϕ and C_ϕ appropriate to each ϕ with axial velocity now appearing as u_3 in the straight axial co-ordinate direction ζ_3 .

The production rate P of turbulence kinetic energy is now written as

$$P = -\overline{\rho u'_1 u'_3} \partial u_3 / h_1 \partial \zeta_1 - \overline{\rho u'_2 u'_3} \partial u_3 / h_2 \partial \zeta_2 \quad (15)$$

and the turbulent shear stresses as

$$\overline{\rho u'_1 u'_3} = -\mu_t \partial u_3 / h_1 \partial \zeta_1 \quad (16)$$

$$\overline{\rho u'_2 u'_3} = -\mu_t \partial u_3 / h_2 \partial \zeta_2 \quad (17)$$

with μ_t given by equation (5).

3. THE NUMERICAL SOLUTION

3.1. The orthogonal curvilinear mesh

The p.d.t. equation (13) was solved by finite differences on a mesh of orthogonally intersecting grid lines in three dimensions. In the cross-plane of the passage the grid lines are

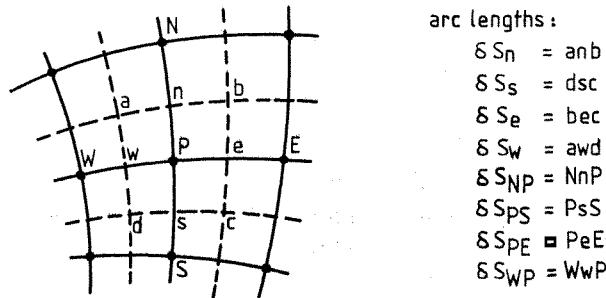


Figure 3. The grid control volumes

curvilinear and intersect orthogonally with each other and with the passage boundaries. The grid nodes are at the points of intersection, through which pass the straight axial lines which complete the three dimensional mesh. A portion of a typical cross-plane mesh is shown in Figure 3 which also shows the contiguous control volumes or 'cells' surrounding each grid node. The boundaries of these cells, shown with broken lines, are formed in the cross-plane by a mesh of lines representing axial planes, mid-way between the main grid lines, and in the axial plane by a pair of cross-sectional planes. A typical grid node is denoted by *P* in Figure 3, its nearest neighbours by *N*, *S*, *E*, *W* and the intersections between control volume faces and grid lines as *n*, *s*, *e*, *w*. These letters are used as suffices to denote the value of a variable at that location.

3.2. Interior control volumes

The finite difference equivalent of equation (13) was obtained by integrating each term over the control volume, using central differencing and linearizing the source term. This micro-integration technique helps to ensure that the resulting finite difference equations satisfy the relevant conservation principles and was carried out so that all the required areas and volumes were obtained in terms of curvilinear arc lengths δS in the mesh. These integrals led to the following standard finite difference equations expressing ϕ_P , the value of ϕ at each location, in terms of the values at the nearest neighbouring nodes i.e.

$$A_P \phi_P = A_N \phi_N + A_S \phi_S + A_E \phi_E + A_W \phi_W + F \tag{18}$$

where coefficients A_N, A_S etc. are of the form

$$\left. \begin{aligned} A_N &= \alpha_n D_\phi \delta S_n / \delta S_{NP} \\ A_E &= \alpha_e D_\phi \delta S_e / \delta S_{PE} \\ \text{etc.} \\ A_P &= A_N + A_S + A_E + A_W - g \end{aligned} \right\} \tag{19}$$

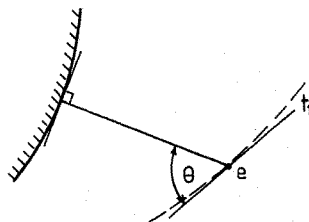


Figure 4. Orientation of grid line tangents

with the source term linearized and written as

$$C_\phi = g\phi_P + F \quad (20)$$

The internodal arc lengths δS_{NP} , δS_{PE} etc. and the cell face arc lengths δS_n , δS_e etc. are shown in Figure 3.

The α coefficients in equations (19) contain the proportion of diffusion factor B appropriate for that location according to the orientation of the local grid line tangent to the normal from the nearest boundary surface passing through that point. A typical grid line tangent is shown as t_1 for location e in Figure 4. For the angle θ shown, the proportion α_e was assumed to be given by the function:²⁰

$$\alpha_e = \cos^2 \theta + (1 + B) \sin^2 \theta \quad (21)$$

3.3. Near boundary control volumes

Passage boundaries were assumed to be either symmetry planes or smooth walls. At the former, the normal gradients of all dependent variables will be zero. At the latter, although all the variables usually assume known values (e.g. velocity is zero), wall functions were used to match the interior solution to the wall conditions. This avoided the large number of grid lines that would otherwise be necessary in this region of high gradients. These functions were applied to the cell next to the wall which was assumed to be a region of constant shear in local equilibrium. This led to conventional wall functions in which the local shear stress τ_s was given by

$$\tau_s = \rho u_3^* C_\mu^{1/4} k^{1/2} \quad (22)$$

where the local friction velocity u_3^* was given by the well known 'log law' (e.g. Schlichting²⁸)

$$u_3^* = u_3 \kappa / \ln(ES^+) \quad (23)$$

in which κ and E are constants and

$$S^+ = C_\mu^{1/4} k^{1/2} \delta S_m / \nu \quad (24)$$

δS_m is the distance normal to the wall and ν the fluid kinematic viscosity. This value of τ_s was assumed to apply at the wall-side control volume face.

The near-wall value of turbulence kinetic energy was obtained as for the interior control volumes with diffusion to the wall set to zero and the production and dissipation calculated from τ_s .

The near-wall value of ε was obtained by neglecting transport of ε by diffusion and assuming a length scale that varied linearly with δS_m ¹⁶ so that

$$\varepsilon = u_3^{*3} / \kappa \delta S_m \quad (25)$$

This value was imposed directly at the near-wall node i.e. the finite difference equation was not used there.

3.4. Empirical constants

The values of the empirical constants used were mainly taken from previous work⁷ and were assumed universal to all passage geometries; they were: $C_\mu = 0.09$, $\sigma_k = 1.0$, $\sigma_\varepsilon = 1.22$, $C_{\varepsilon 1} = 1.55$, $C_{\varepsilon 2} = 2.0$, $E = 9.02$, $\kappa = 0.42$.

3.5. The solution method

The finite-difference equations were solved with an iterative line-by-line back-substitution method based on the tri-diagonal matrix (Thomas) algorithm (e.g. Ames²⁹) and arranged to operate in alternating directions across the mesh. Block adjustment (e.g. Ames²⁹) was also applied to speed convergence of the solution. The finite difference equations for u_3 , k and ε were solved in sequence and the stresses updated after each sequence.

The numerical solution was assumed converged when the sum of the absolute axial momentum sources over the field was less than 0.001 of the axial momentum flux. Reduction of the residual sources below this gave negligible changes to the solution. Discretization errors were minimized in the present work by using the meshes and differencing methods selected⁷ after a comprehensive series of accuracy tests which included grid refinement, comparisons between solutions with different orthogonal meshes, extensive comparisons of laminar flow calculations with analytical solutions and symmetry tests with turbulent flow. Details of these tests can be found in Rapley.³⁰

4. PREDICTIONS

The local mean flow characteristics of passage flows are represented by the distributions of local wall shear stress τ_s and axial velocity u_3 . The former is normalized with the peripherally averaged wall shear stress $\bar{\tau}_s$ given by

$$\bar{\tau}_s = (1/M) \int_0^M \tau_s dM = (dp/d\zeta_3) D_e/4 \quad (26)$$

where M is the passage wall perimeter, $dp/d\zeta_3$ the axial pressure gradient and D_e the equivalent diameter. Axial velocity is normalized with the mean velocity \bar{u}_3 given by

$$\bar{u}_3 = (1/A) \int_0^A u_3 dA \quad (27)$$

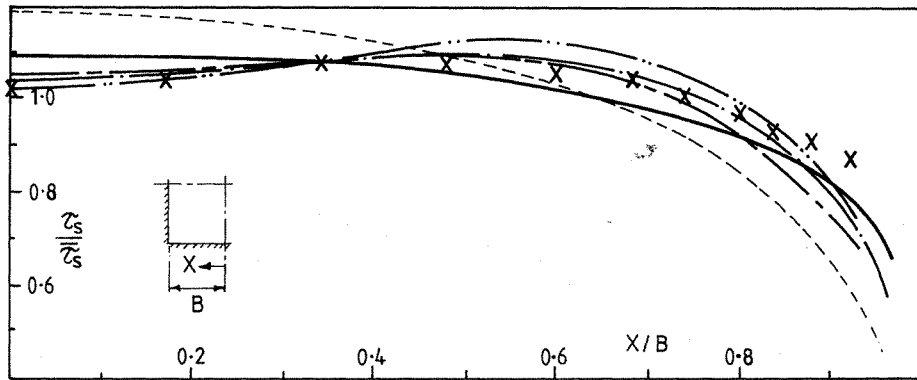
where A represents the passage flow area. The axial pressure gradient is represented by the dimensionless wall shear stress or friction factor f where

$$f = \bar{\tau}_s / (\rho \bar{u}_3^2 / 2) \quad (28)$$

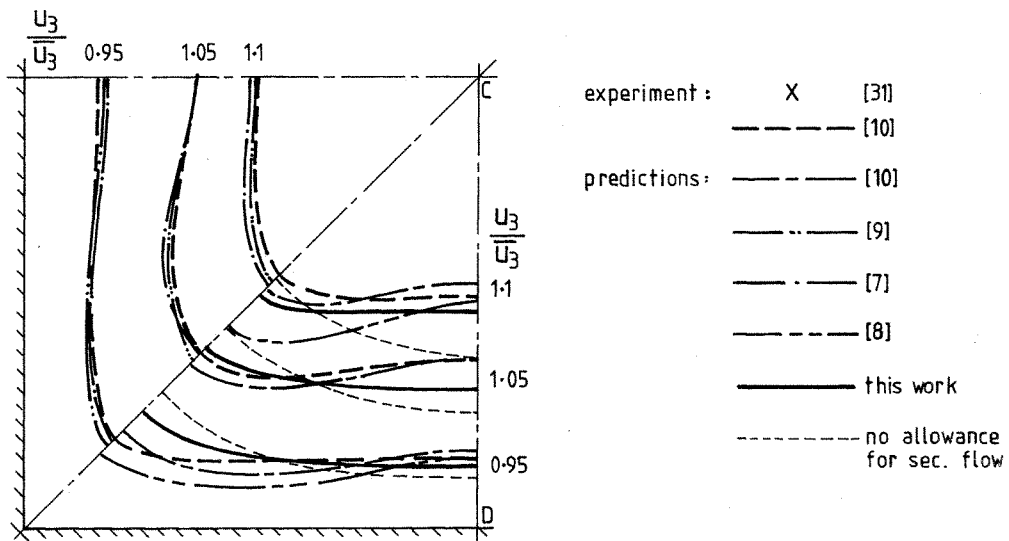
4.1. Square duct

This duct provided a useful test case since extensive measurements are available and many previous authors have applied their duct flow calculation methods to this case. A 12×12 Cartesian mesh was used in a duct symmetry quadrant with a variable spacing grid to give more nodes in the wall region.

The present predictions of wall shear stress and axial velocity are compared with experiment and previous predictions in Figure 5 which also shows the predictions with no allowance for secondary flow (i.e. $B = 0$). Compared with the latter, all predictions are seen to be in reasonable agreement with experiment and show the accepted main effects of secondary flow in that wall shear stress is made more uniform and axial velocity contours bulge into the duct corners. Further inspection will reveal that some of the detail has, however, not been predicted by the present method. In particular the level of wall shear stress at mid-wall is a little high and the slight bulging of axial velocity contours away from the wall in the mid-wall symmetry plane (CD in Figure 5(b)) is missing. Both of these effects



(a) Wall shear stress, $Re = 3.4 \times 10^4$



(b) Axial velocity, $Re = 2.15 \times 10^5$

Figure 5. Square duct mean flow

are likely to be due to convection of the mid-wall region fluid away from the wall by the recirculating secondary flow (see Figure 1(a)). This deficiency in simulating transport effects of secondary flow away from the wall is not unexpected however, since the simplifications made in the present method were based on secondary flow transport parallel to the wall.

The predicted friction factor characteristics for square ducts are shown in Figure 6 compared with experiment. The present prediction is in reasonable agreement with experiment and an improvement on most of the previous predictions. It is of interest to note that the Blasius empirical equation for circular ducts represents the experimental data for square ducts very well, implying that the equivalent diameter concept is valid for friction factors in this duct.

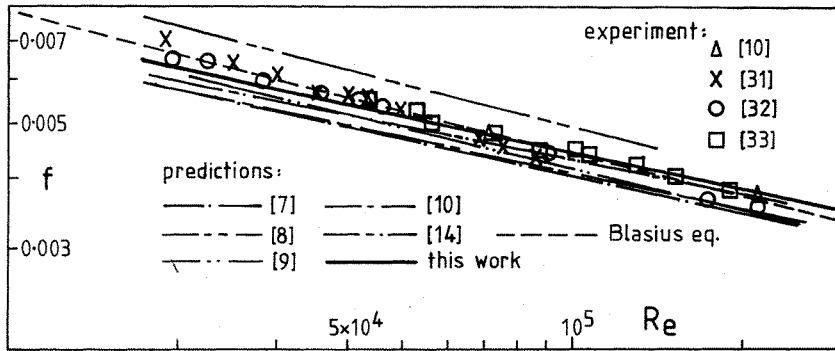
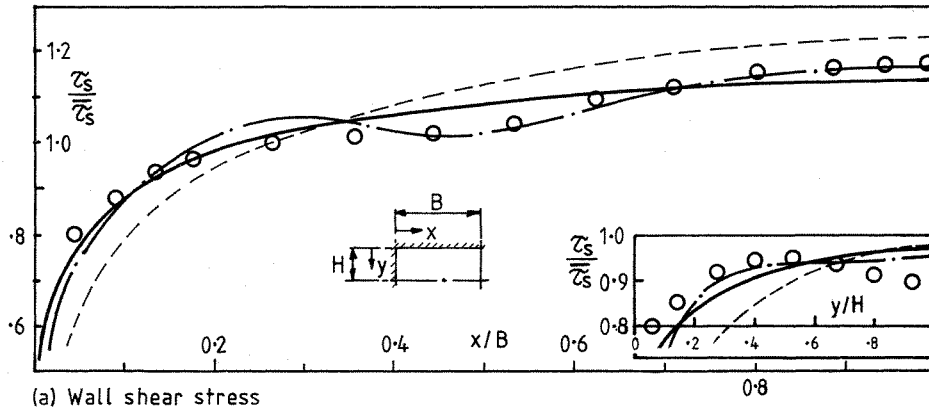


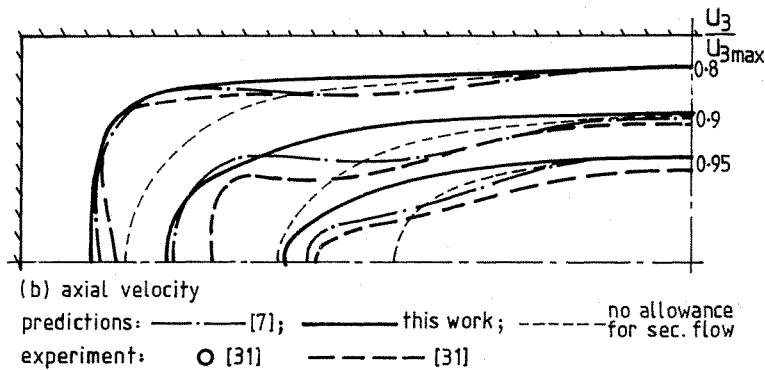
Figure 6. Square duct friction factor characteristics

4.2. Rectangular duct

A 22×12 Cartesian mesh was used for calculations in the quadrant of a rectangular duct of 3:1 aspect ratio. The present predictions are compared in Figure 7 with the experiments of Leutheusser³¹ and the calculations of Gosman and Rapley⁷ which appear to be the only previous predictions available for this duct. The secondary flow circulations measured by Gessner and Jones³ in a rectangular duct are sketched in Figure 1(b).



(a) Wall shear stress



(b) axial velocity

Figure 7. Rectangular duct mean flow with $Re = 5.6 \times 10^4$

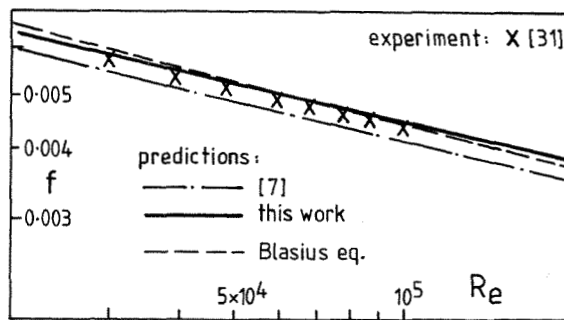


Figure 8. Rectangular duct friction factor characteristics

As noted in the square duct case, and here most apparent in the axial velocity contours, some of the detailed effects due to secondary flow transport normal to the duct walls have not been predicted as well as with the Gosman and Rapley method where secondary flows were calculated. However, compared with the calculations made with no secondary flow effect, the present predictions appear to have simulated the main effects quite well.

The predicted friction factor characteristic is seen in Figure 8 to be in fair agreement with experiment and an improvement on the prediction of Gosman and Rapley. Friction factors are seen to be slightly overpredicted by the equivalent diameter concept.

4.3. Elliptical duct

Elliptical cylindrical co-ordinates were used to generate an orthogonal curvilinear mesh for the quadrant of an elliptical duct, as shown typically in Figure 9. In this co-ordinate system, Cartesian co-ordinates x_1 and x_2 are related to the curvilinear co-ordinates ζ_1 and ζ_2 by

$$\left. \begin{aligned} x_1 &= C_0 \cosh \zeta_1 \cos \zeta_2 \\ x_2 &= C_0 \sinh \zeta_1 \sin \zeta_2 \end{aligned} \right\} \quad (29)$$

where C_0 is a constant depending on duct aspect ratio (a/b in Figure 9).

The predicted wall shear stress and axial velocity profiles for a duct of 2.0 aspect ratio are compared with experiment in Figure 10. The calculations of Cain *et al.*³⁷ neglected secondary flow and assumed isotropic eddy viscosities based on Van Driest type mixing lengths. The

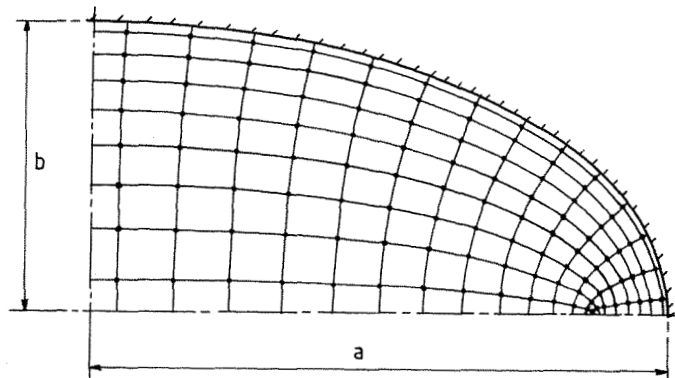
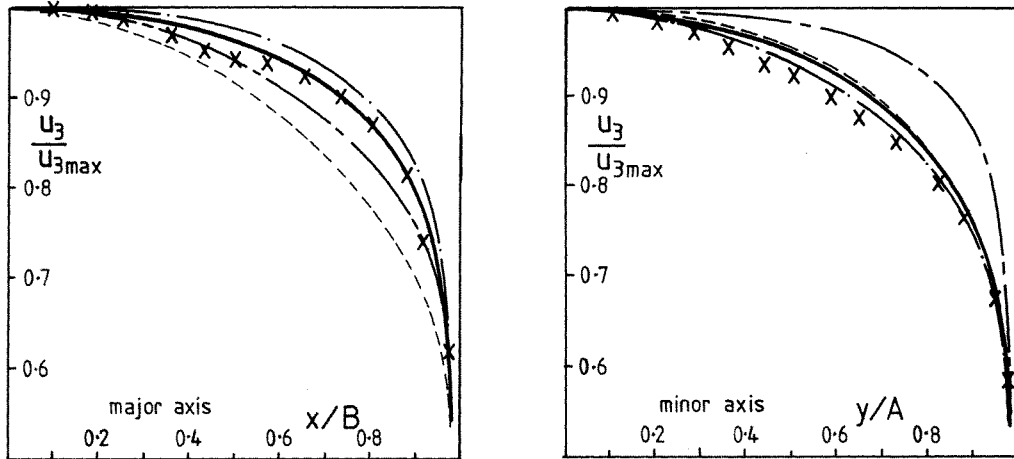
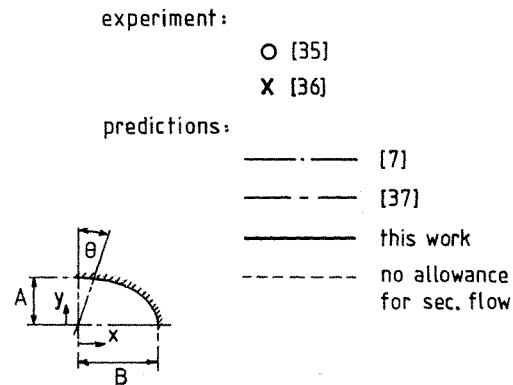
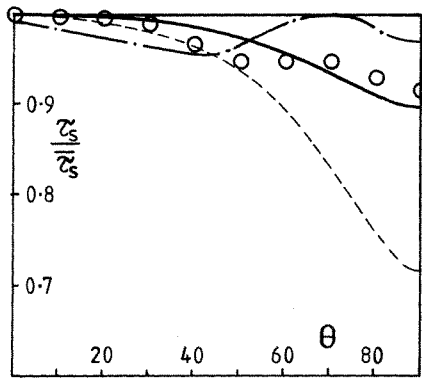


Figure 9. Orthogonal grid for elliptical ducts



(a) Axial velocity, $R = 1.2 \times 10^5$



(b) Wall shear stress, $R_e = 1.2 \times 10^5$

Figure 10. Elliptical duct mean flow

present predictions are seen to be in reasonable agreement with experiment and a considerable improvement on those of Cain *et al.* and are at least as acceptable as those of Gosman and Rapley which appear to be the only previous calculations available where secondary flows were calculated. The secondary flow effects on the predictions are quite dramatic with a reduction of peripheral shear stress variation from nearly 30 per cent to about 10 per cent which is close to the experimental variation of $8\frac{1}{2}$ per cent.

When compared with the predictions with no secondary flow effect the increase in wall stress near the major axis plane ($\theta = 90^\circ$) is consistent with the increased axial velocity along the major axis plane and is most probably due to the convective transport of core fluid towards the wall along the major axis plane by secondary flow. There is a lesser effect of a lower level of axial velocity along the minor axis plane apparent in the predictions which is most likely due to the recirculating secondary flow convecting wall region fluid towards the core. This implied secondary flow circulation pattern is in agreement with that predicted by

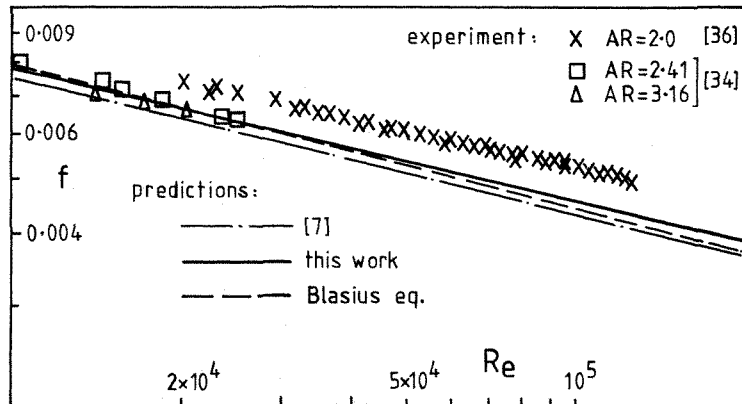


Figure 11. Elliptical duct friction factor characteristics

the Gosman and Rapley method but cannot be confirmed by experiment since no measurements of secondary flow appear as yet to be available. The absence of the above implied secondary flow effects on local axial velocity levels is most exaggerated in the predictions of Cain *et al.* and is further evidence of the necessity to include these effects in passage flow calculations.

Figure 11 compares calculated and experimental friction factors for ducts of aspect ratio 2.0 and greater. The present method is seen to underpredict the measurements of Cain *et al.*³⁶ by about 10 per cent whereas it is in reasonable agreement with the more limited measurements of Barrow and Roberts.³⁴ The former measurements are significantly higher than values from the Blasius equation for circular pipes which is perhaps surprising since the elliptical shape is not too far removed from circular with, as previously noted, only a small peripheral variation in wall shear stress. This is in contrast to rectangular ducts where, with sharp corners, there is a much greater variation in wall shear stress (see Figure 7) and yet the measured friction factors are fairly close to the Blasius equation. The measurements of Barrow and Roberts for elliptical ducts of higher aspect ratio than 2.0 are near the Blasius equation perhaps implying that those of Cain *et al.* may be uncharacteristically high, due probably to effects such as incomplete flow development, tube surface roughness and inaccuracies in duct alignment etc; few details were given by the authors.

4.4. Rod bundle channel

With its important application in nuclear reactor cores, this passage shape has received much attention from both experimenters and numerical analysts. A numerically generated 16×10 orthogonal curvilinear mesh, similar to that shown in Figure 12 was used for

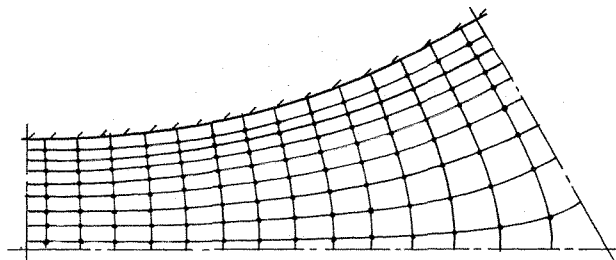


Figure 12. Orthogonal grid for rod bundles channels

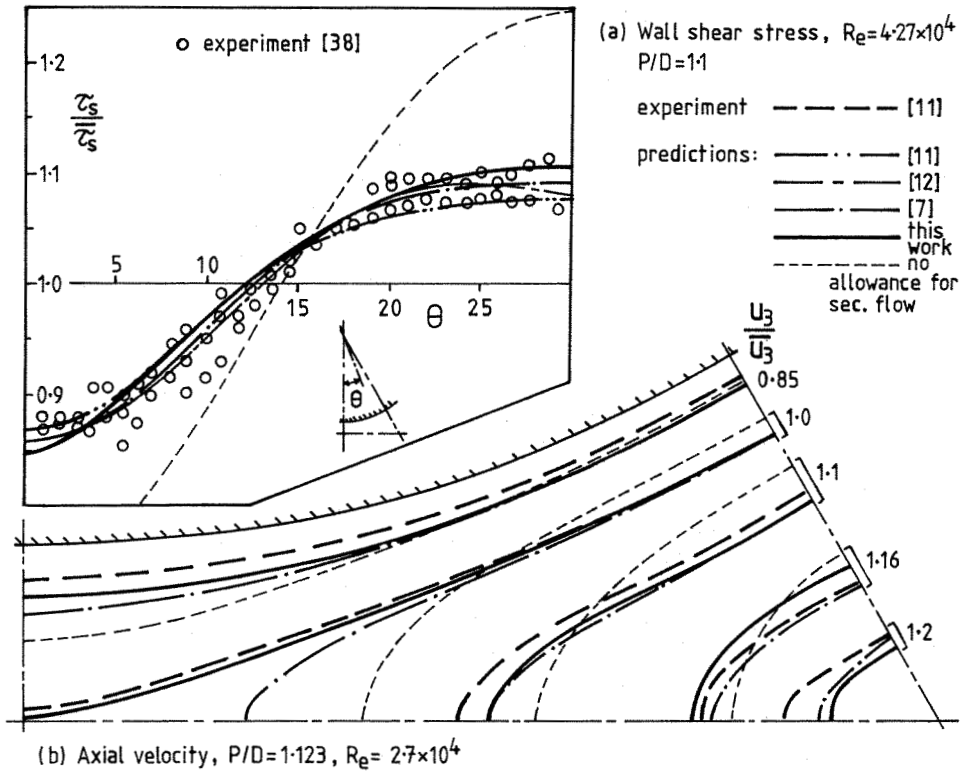


Figure 13. Rod bundle channel mean flow

calculations in symmetry sub-channels of equilateral triangular infinite arrays with rod pitch/diameter (P/D) ratios of 1.1 and 1.123. The conformal mesh generation method used can be applied to a wide range of passage shapes and employs finite differences to solve a pair of Laplace equations which relate the Cartesian and general orthogonal co-ordinate frames—details of the procedure can be found in Rapley.³⁰

Predictions are compared with experiment in Figure 13 which shows in 13(a) the present and all previous predictions of wall shear stress to be in good agreement with experiment.

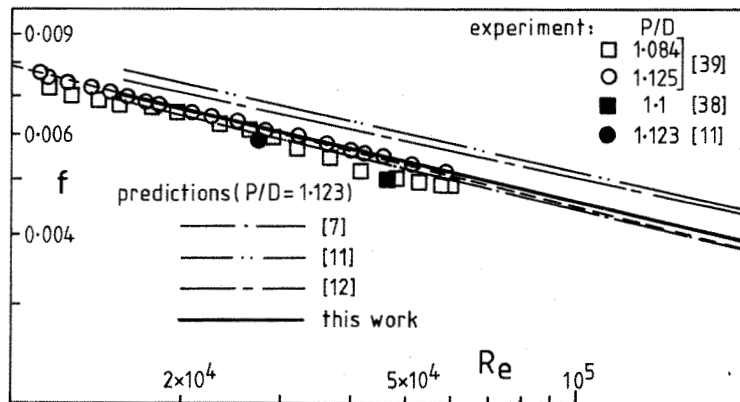


Figure 14. Rod bundle channel friction factor characteristics

The effects of secondary flow in making the wall shear stress profile more uniform are well simulated. The calculated axial velocity contours from the present method are also in good agreement with experiment and generally at least as good as predictions from the more complex method of Gosman and Rapley.⁷ The effects of secondary flow in making the axial velocity contours bulge into the gap region (closest approach of rods) are quite closely simulated by the present method.

The friction factor characteristics from the present method are seen in Figure 14 to be in reasonable agreement with the experimental data and an improvement on some of the previous predictions.

5. CONCLUSIONS

The foregoing comparisons have shown the present method to be capable of simulating the main effects of secondary flow, producing acceptable local mean flow predictions for fully developed turbulent flow in a range of passage shapes. In some cases, the detail has not been predicted as well as with other more complex procedures, due mainly to the loss of some of the transport effects of secondary flow normal to the passage walls by the assumptions made in formulating the method. This slight loss in detail is not serious and is accepted as a not-too-severe penalty for the large simplifications made in eliminating solution of the cross-plane momentum and continuity equations. These simplifications have the benefit of removing the stability and convergence problems inherent in the more complex methods where the recirculating secondary flow is calculated and of reducing the required storage and CPU time. A typical CPU time for a rod bundle channel solution, including generation of the grid, is 7.6 min on an ICL 2950 digital computer which is, for example, only one third of the CPU time required for an equivalent calculation including secondary flow with the six p.d.t. method of Gosman and Rapley.⁷

Finally, it is perhaps of interest to note that calculation methods employing anisotropic turbulent viscosities and ignoring secondary flow are unlikely to achieve detailed accuracy in the prediction of local mean flow in passages. The present work and results from previous work in which secondary flows were calculated indicate that anisotropic eddy viscosities may have only a minor influence on local mean flow distributions compared with that of secondary flow. Thus any shortcomings in the detailed predictions of local mean flow using anisotropic eddy viscosities only are likely to be due to the absence of convective secondary flow transport effects rather than failure to properly allow for anisotropy in diffusion transport.

REFERENCES

1. B. E. Launder and W. M. Ying, 'Secondary flows in ducts of square cross-section' *J. Fluid Mech.*, **37**, 289 (1972).
2. E. Brundrett and W. D. Baines, 'The production and diffusion of vorticity in duct flow', *J. Fluid Mech.*, **19**, 375 (1964).
3. F. B. Gessner and J. B. Jones, 'On some aspects of fully developed turbulent flow in rectangular channels', *J. Fluid Mech.*, **23**, 689 (1965).
4. A. M. M. Aly, A. C. Trupp and A. D. Gerrard, 'Measurement and prediction of fully developed turbulent flow in an equilateral triangular duct', *J. Fluid Mech.*, **85**, 57 (1978).
5. J. Nikuradse, 'Investigations on the distribution of velocity in turbulent flow' (in German), *VDI-Forschungsheft*, 281 (1926).
6. J. Nikuradse, 'Turbulent flow in non-circular shaped pipes', (in German), *Ing.-Arch.*, **1**, 306 (1930).
7. A. D. Gosman and C. W. Rapley, 'Fully developed flow in passages of arbitrary cross-section', in *Recent Advances in Numerical Methods in Fluids*, (Eds. C. Taylor and K. Morgan), Pineridge Press, Swansea, 1980.
8. D. Naot, A. Shavit and M. Wolfshtein, 'Numerical calculations of Reynolds stresses in a square duct with secondary flow', *Wärme-und-Stoff.*, **7**, 151 (1974).

9. G. Reece, 'A generalised Reynolds stress model of turbulence', *Ph.D. Thesis*, University of London, 1977.
10. B. E. Launder and W. M. Ying, 'Prediction of flow and heat transfer in ducts of square cross-section', *Proc. I. Mech. E.*, **187**, 455 (1973).
11. P. Carajilescov and N. E. Todreas, 'Experimental and analytical study of axial turbulent flows in an interior sub-channel of a bare-rod bundle', *J. Heat transfer, Trans. ASME*, **98**, 262 (1976).
12. A. C. Trupp and A. M. M. Aly, 'Predicted turbulent flows in triangular array rod bundles', *Trans. ASME*, **101**, 354 (1979).
13. S. Neti and R. Eichhorn, 'Computation of developing turbulent flow in a square duct', *Proc. ASME Symp. Turb. B. Layers*, Niagara Falls (1979).
14. F. B. Gessner and A. F. Emery, 'The numerical prediction of developing turbulent flow in rectangular ducts', *Proc. 2nd Symp. Turb. shear flows*, Imperial College, London, 17.1 (1979).
15. F. B. Gessner and A. F. Emery, 'A Reynolds stress model for turbulent corner flows, Part I', *J. Fluid Eng., Trans. ASME* **76-FE-C** (1976).
16. B. E. Launder and D. B. Spalding, *Mathematical Models of Turbulence*, Academic Press, London, 1972.
17. N. I. Buleev, 'Theoretical model of the Mechanism of turbulent exchange in fluid flows', *AERE Trans.*, 957 (1963).
18. B. E. Launder and D. B. Spalding, 'The numerical computation of turbulent flows', *Comp. Meth. in App. Mech. and Eng.*, **3**, 269 (1974).
19. V. Vonka and B. H. Boonstra, 'Calculated heat transfer development in bundles', *Nuclear Eng. & Design*, **31**, 337 (1974).
20. R. Meyder, 'Turbulent velocity and temperature distributions in the central sub-channel of rod bundles', *Nuclear Eng. & Design*, **35**, 181 (1975).
21. H. Ramm and J. Johannsen, 'A phenomenological turbulence model and its application to heat transport in infinite rod arrays with axial turbulent flow', *J. Heat Trans., Trans. ASME*, **97**, 231 (1975).
22. K. Rehme, 'Anisotropic eddy viscosities in the turbulent flow through a rod bundle', *Proc. Symp. Turb. Shear Flows*, Penn, State Uni., 8.41 (1977).
23. B. Kjellstrom, 'Studies of flow parallel to a rod bundle of triangular array', *Report AE/RV/196*, AB Atomenergi, Sweden (1971).
24. P. Carajilescov, 'Experimental and analytical study of axial turbulent flows in an interior sub-channel of a bare-rod bundle', *Ph.D. Thesis*, M.I.T., USA (1975).
25. R. Nijsing and W. Eifler, 'Temperature fields in liquid-metal-cooled rod assemblies', *Progress in Heat & Mass Transfer*, **7**, 115 (1973).
26. W. C. Reynolds and T. Cebeci, 'Calculation of turbulent flows', in *Turbulence* (Ed. P. Bradshaw), Springer-Verlag, 1978.
27. S. B. Pope, 'The calculation of turbulent recirculating flows in general orthogonal co-ordinates', *J. Comp. Physics*, **26**, 197 (1978).
28. H. Schlichting, *Boundary Layer Theory*, 7th Edn., McGraw-Hill, New York, 1979.
29. F. A. Ames, *Numerical Methods for Partial Differential Equations*, Academic Press, New York, 1977.
30. C. W. Rapley, 'Fluid and heat flow in tubes of arbitrary cross-section', *Ph.D. Thesis*, University of London, 1980.
31. H. J. Leutheusser, 'Turbulent flow in rectangular ducts', *Proc. ASCE J. Hy. Div.*, **89**, 1 (1963).
32. J. P. Hartnett, J. Koh and S. T. McComas, 'A comparison of predicted and measured friction factors for turbulent flow through rectangular ducts', *Trans. ASME*, **84**, 82 (1962).
33. D. L. Thomas and P. G. Easter, 'Measurements of wall shear stress in a duct of square cross-section', *CEGB Report RD/B/N2477* (1972).
34. H. Barrow and A. Roberts, 'Flow and heat transfer in elliptical ducts', *Paper No. FC4.1, 4th Int. Heat Trans. Conf.*, Paris, (1970).
35. J. Duffy and D. Cain, 'On the use of the Preston tube in elliptical ducts', *Aero. J.*, **76**, 371 (1972).
36. D. Cain and J. Duffy, 'An experimental investigation of turbulent flow in elliptical ducts', *Int. J. Mech. Science*, **13**, 451 (1971).
37. D. Cain, A. Roberts and H. Barrow, 'A theoretical study of fully developed flow and heat transfer in elliptical ducts', *Paper No. C120/72, Proc. I. Mech. E. Conf. Compact Heat Ex.* (1972).
38. V. I. Subbotin *et al.*, 'Velocity field of turbulent fluid flow in a longitudinal streamline of clusters of rods', *AEC-tr-7189* (1971).
39. K. Rehme, 'Pressure drop performance of rod bundles in hexagonal arrangements', *Int. J. Heat Mass Trans.*, **15**, 2499 (1972).